Front. Phys. China, 2010, 5(3): 291–307
DOI 10.1007/s11467-010-0005-y

REVIEW ARTICLE

Manipulate light polarizations with metamaterials: From microwave to visible

Jia-ming HAO (郝加明)[1,2], **Min QIU** (仇旻)[2], **Lei ZHOU** (周磊)[1,†]

[1] *Surface Physics Laboratory (State Key Laboratory) and Physics Department, Fudan University, Shanghai 200433, China*
[2] *Laboratory of Photonics and Microwave Engineering, School of Information and Communication Technology, Royal Institute of Technology (KTH), Electrum 229, 164 40, Kista, Sweden*
E-mail: phzhou@fudan.edu.cn

Received January 14, 2010; accepted March 12, 2010

Polarization is an important characteristic of electromagnetic (EM) waves, and efficient manipulations over EM wave polarizations are always desirable in practical applications. Here, we review the recent efforts in controlling light polarizations with metamaterials, at frequencies ranged from microwave to visible. We first presented a 4×4 version transfer matrix method (TMM) to study the scatterings by an anisotropic metamaterial of EM waves with arbitrary propagating directions and polarizations. With the 4×4 TMM, we discovered several amazing polarization manipulation phenomena based on the reflection geometry and proposed corresponding model metamaterial systems to realize such effects. Metamaterial samples were fabricated with the help of finite-difference-time-domain (FDTD) simulations, and experiments were performed to successfully realize these ideas at both microwave and visible frequencies. Efforts in employing metamaterials to manipulate light polarizations based on the transmission geometry are also reviewed.

Keywords polarization, metamaterials

PACS numbers 42.25.Bs, 42.25.Ja, 78.20.Bh

Contents

1 Introduction

Polarization is conventionally described by the oscillating behaviors of the $\boldsymbol{E}$ vectors in a wave [1–4]. If the trajectory of the end point of $\boldsymbol{E}$ vector forms a line (circle, ellipse) on the wave front as time varies, the wave is called linearly (circularly, elliptically) polarized. Polarized lights have important applications in different areas of scientific research, including biology, chemistry, astronomy, and physics. Practically, it is highly desirable to have full control of the wave polarizations. Several conventional methods are available to manipulate the wave polarizations. For example, by using two wave plates, one can convert the light polarization completely from one direction to its cross direction. Also, a linearly polarized light can be generated when a natural light passes through an optical grating or reflected by a medium at the Brewster angle. Other polarization-related phenomena include the optical activity, the birefringence effects, the polarization beam splitting, etc. [1–4]. While these conventional methods have their own characteristics and merits, they do suffer some limita-

tions simultaneously. For example, these devices are typically not totally reflective or transparent so that some optical signals are inevitably lost during operation. In addition, many conventional devices are much thicker than wavelength, making the systems bulky for longer wavelength applications.

Metamaterials are artificial electromagnetic materials composed by subwavelength local resonance structures of electric and/or magnetic type and thus possess arbitrary values of permittivity ε and permeability μ dictated by such resonance structures [5–12]. Many novel EM properties were predicted or discovered based on metamaterials, including the negative refraction [13–15], the superlensing effect [16–19], reversed Doppler shift [13, 20–22], abnormal Cherenkov radiation [13, 23–26], the subwavelength metamaterial cavities [27–29], etc. In particular, combining with the transformation optics method [30–32], a lot of intriguing wave-functional devices have been proposed, including the invisibility cloaks [30, 31], electromagnetic field concentrators [33], field rotators [34], cylindrical superlenses [35], and superscatterer [36].

Now, that metamaterials can in principle possess arbitrary values of ε and μ, it is quite natural to ask whether they could have better controls over EM wave polarizations. Recently, there were indeed quite some attempts to employ such new materials to control EM wave polarizations [37–47], with several fascinating phenomena discovered. In what follows, we will give a detailed review on these efforts.

In the next section, we first generalize the conventional 2×2 transfer-matrix method (TMM) to a 4×4 version. This is because metamaterials are usually anisotropic [6–12], and many exciting polarization-related phenomena appear in the general situations where the incident EM wave takes arbitrary propagation direction and polarization. Theoretical calculations for such a general case are much more complicated than that for the isotropic case and for the simplified anisotropic problems (either $\boldsymbol{E}$ or $\boldsymbol{H}$ field is along one of the optical axes) [48–53]. For the latter two cases, one can always write down the wave solution as a combination of two independent modes, i.e., the s and p modes, with electric or magnetic field parallel to a prefixed planar interface. Polarizations are conserved as EM wave passes across the interface for each mode, and therefore, one can study the propagations of the two modes separately employing the standard 2×2 TMM [54, 55]. However, the same thing cannot be done in a general anisotropic problem, and thus, the standard 2×2 TMM should be generalized to a 4×4 version when we consider the wave transmissions/reflections in such a situation. While formalisms were previously available for an anisotropic medium with an anisotropic $\vec{\vec{\varepsilon}}$ tensor [54], those formulas cannot be directly applied to the present metamaterial problems where both $\vec{\vec{\varepsilon}}$ and $\vec{\vec{\mu}}$ could be anisotropic tensors.

In Section 3, we review our efforts in employing anisotropic metamaterials to manipulate wave polarizations under the reflection geometry. We discovered several amazing polarization manipulation phenomena in different systems and then proposed realistic metamaterial structures that can realize such effects. For example, by shining a linearly polarized EM wave on a specific metamaterial, we found that all kind of polarization states (circular, elliptic, and linear) are realizable after reflections under different conditions. We also found it possible to rotate the polarization direction of a linearly polarized EM wave by an arbitrary angle and even convert it to its cross direction completely. Several theoretical predictions were experimentally verified at both microwave and visible frequencies.

After we briefly review the efforts in employing metamaterials to manipulate light polarizations under the transmission geometry in Section 4, we conclude the paper in Section 5.

2 Computational methodology

In this section, we establish the 4×4 version of TMM. Consider a stratified medium consisting of homogeneous but anisotropic metamaterial layers, with the z axis chosen normal to the interfaces, as shown in Fig. 1.

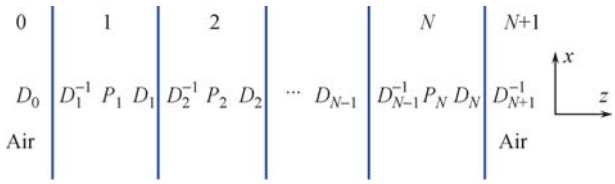

Fig. 1 Geometry of a stratified structure consisting of N layers of anisotropic metamaterials embedded inside air.

2.1 The 4×4 transfer matrix

We start from studying the propagations of plane waves in a homogeneous anisotropic medium, with permittivity tensor and permeability tensor given by

$$\vec{\vec{\varepsilon}} = \begin{pmatrix} \varepsilon_x & 0 & 0 \\ 0 & \varepsilon_y & 0 \\ 0 & 0 & \varepsilon_z \end{pmatrix}, \quad \vec{\vec{\mu}} = \begin{pmatrix} \mu_x & 0 & 0 \\ 0 & \mu_y & 0 \\ 0 & 0 & \mu_z \end{pmatrix} \tag{1}$$

According to the Maxwell equations, the $\boldsymbol{E}$ field inside such a medium should satisfy

$$\boldsymbol{k} \times [(\vec{\vec{\mu}}^{-1}) \cdot (\boldsymbol{k} \times \boldsymbol{E})] + \frac{\omega^2}{c^2} \vec{\vec{\varepsilon}} \cdot \boldsymbol{E} = 0 \tag{2}$$

where ω and $\boldsymbol{k}$ denote the angular frequency and wave vector, respectively. With k_x and k_y prefixed and applying the constrain $\nabla \cdot (\vec{\vec{\varepsilon}} \cdot \boldsymbol{E}) = 0$, the dispersion relation between ω and k_z is found as:

$$\left(\frac{\omega}{c}\right)^4 \varepsilon_x\varepsilon_y\varepsilon_z - \left[\sum_{i\neq j\neq l} \varepsilon_i(\varepsilon_j\mu_j^{-1} + \varepsilon_l\mu_l^{-1})k_i^2\right]\left(\frac{\omega}{c}\right)^2 + \left(\frac{1}{2}\sum_{i\neq j\neq l} \mu_i^{-1}\mu_j^{-1}k_l^2\right)\sum_i \varepsilon_i k_i^2 = 0 \quad (3)$$

where $i, j, l = x, y, z$. Equation (3) has four roots, denoted by $\{k_{z1}, k_{z2} = -k_{z1}, k_{z3}, k_{z4} = -k_{z3}\}$ and corresponding to two independent modes propagating forwardly and backwardly. For each solution, the electric field distribution can be obtained through solving Eq. (2) with the solution of k_z inserted. In general, the wave solution inside the anisotropic medium must be a linear combination of these four modes, so that the EM waves can be expressed as:

$$\begin{pmatrix} \boldsymbol{E}^{(n)} \\ \boldsymbol{H}^{(n)} \end{pmatrix} = \sum_{\sigma=1}^{4} E_\sigma^{(n)} \begin{pmatrix} \hat{e}_\sigma^{(n)} \\ \hat{h}_\sigma^{(n)} \end{pmatrix} \mathrm{e}^{-\mathrm{i}[k_x x + k_y y + k_{z\sigma}^{(n)}(z - z_n) - \omega t]} \quad (4)$$

where $\{E_1^{(n)}, E_2^{(n)}, E_3^{(n)}, E_4^{(n)}\}$ is a set of expansion coefficients to be determined, $\hat{e}_\sigma^{(n)}, \hat{h}_\sigma^{(n)}, k_{z\sigma}^{(n)}$ are the field vectors and wave-vectors calculated in the nth layer, and z_n is the starting position of the nth layer. Imposing the condition that the tangential components of $\boldsymbol{E}$ and $\boldsymbol{H}$ are continuous at the boundary $z = z_{n+1}$, we found that

$$\begin{pmatrix} E_1^{(n+1)} \\ E_2^{(n+1)} \\ E_3^{(n+1)} \\ E_4^{(n+1)} \end{pmatrix} = D_{n+1}^{-1} D_n P_n \begin{pmatrix} E_1^{(n)} \\ E_2^{(n)} \\ E_3^{(n)} \\ E_4^{(n)} \end{pmatrix} = M_{n+1,n} P_n \begin{pmatrix} E_1^{(n)} \\ E_2^{(n)} \\ E_3^{(n)} \\ E_4^{(n)} \end{pmatrix} \quad (5)$$

with

$$D_n = \begin{pmatrix} \hat{e}_1^{(n)}\cdot\hat{y} & \hat{e}_2^{(n)}\cdot\hat{y} & \hat{e}_3^{(n)}\cdot\hat{y} & \hat{e}_4^{(n)}\cdot\hat{y} \\ \hat{h}_1^{(n)}\cdot\hat{x} & \hat{h}_2^{(n)}\cdot\hat{x} & \hat{h}_3^{(n)}\cdot\hat{x} & \hat{h}_4^{(n)}\cdot\hat{x} \\ \hat{h}_1^{(n)}\cdot\hat{y} & \hat{h}_2^{(n)}\cdot\hat{y} & \hat{h}_3^{(n)}\cdot\hat{y} & \hat{h}_4^{(n)}\cdot\hat{y} \\ \hat{e}_1^{(n)}\cdot\hat{x} & \hat{e}_2^{(n)}\cdot\hat{x} & \hat{e}_3^{(n)}\cdot\hat{x} & \hat{e}_4^{(n)}\cdot\hat{x} \end{pmatrix} \quad (6)$$

and

$$P_n = \begin{pmatrix} \mathrm{e}^{-\mathrm{i}k_{z1}^{(n)}d_n} & & & \\ & \mathrm{e}^{-\mathrm{i}k_{z2}^{(n)}d_n} & & \\ & & \mathrm{e}^{-\mathrm{i}k_{z3}^{(n)}d_n} & \\ & & & \mathrm{e}^{-\mathrm{i}k_{z4}^{(n)}d_n} \end{pmatrix} \quad (7)$$

It is noted that in the absence of magnetic anisotropy (i.e., $\mu_x = \mu_y = \mu_z = \mu$), matrices D_n and P_n recover the results obtained previously [Eqs. (17) and (18) in Ref. [57]]. When both the magnetic and electric anisotropy are absent (i.e., $\mu_x = \mu_y = \mu_z = \mu, \varepsilon_x = \varepsilon_y = \varepsilon_z = \varepsilon$), the 4×4 transfer matrix $M_{n+1,n}$ is reduced to two independent 2×2 transfer matrixes, recovering the isotropic medium case [6]. On the other hand, P_n is the usual propagation matrix to describe how EM wave propagates in the nth anisotropic layer (with a distance d_n). Therefore, expansion coefficients in an arbitrary layer (say, the nth layer) can be related to those in the first layer via applying Eq. (5) iteratively,

$$\begin{pmatrix} E_1^{(n)} \\ E_2^{(n)} \\ E_3^{(n)} \\ E_4^{(n)} \end{pmatrix} = M_{n,n-1}P_{n-1}M_{n-1,n-2}P_{n-2}\cdots \cdot M_{2,1}P_1 \begin{pmatrix} E_1^{(1)} \\ E_2^{(1)} \\ E_3^{(1)} \\ E_4^{(1)} \end{pmatrix} \quad (8)$$

and the EM fields in the nth layer can be calculated from Eq. (4) after the expansion coefficients are known.

2.2 Transmission and reflection coefficients

For the system shown in Fig. 1, we label the semi-infinite reference medium on the left (right)-hand side of the system as the 0^{th} [$(N+1)$th] layer (see Fig. 1). Assume a light is incident from the 0^{th} layer, and then, the reflected waves in this layer and the transmitted wave in the last layer can be calculated with the transfer-matrix technique presented above. Apparently, the eigenmodes in the reference medium are just the conventional s and p modes that defined for the isotropic medium [38]. Let E_s^i, E_p^i, E_s^r, E_p^r, and E_s^t, E_p^t denote the complex amplitudes of the s and p modes of the incident, reflected, and transmitted waves, correspondingly. Applying the techniques described previously, the field inside the last layer (determined by the parameters E_s^t and E_p^t) can be associated with those inside the 0^{th} layer (determined by the parameters $E_s^i, E_s^r, E_p^i, E_p^r$) by a transfer matrix as:

$$\begin{pmatrix} E_s^t \\ 0 \\ E_p^t \\ 0 \end{pmatrix} = Q \begin{pmatrix} E_s^i \\ E_s^r \\ E_p^i \\ E_p^r \end{pmatrix} = \begin{pmatrix} Q_{11} & Q_{12} & Q_{13} & Q_{14} \\ Q_{21} & Q_{22} & Q_{23} & Q_{24} \\ Q_{31} & Q_{32} & Q_{33} & Q_{34} \\ Q_{41} & Q_{42} & Q_{43} & Q_{44} \end{pmatrix} \begin{pmatrix} E_s^i \\ E_s^r \\ E_p^i \\ E_p^r \end{pmatrix} \quad (9)$$

where

$$Q = M_{N+1,N}P_N M_{N,N-1}P_{N-1}\cdots M_{2,1}P_1M_{1,0}P_0 \quad (10)$$

The reflection and transmission coefficients can then be

calculated as:

$$r_{ss} = \left.\frac{E_s^r}{E_s^i}\right|_{E_p^i=0} = \frac{Q_{24}Q_{41} - Q_{21}Q_{44}}{Q_{22}Q_{44} - Q_{24}Q_{42}} \tag{11}$$

$$r_{sp} = \left.\frac{E_p^r}{E_s^i}\right|_{E_p^i=0} = \frac{Q_{21}Q_{42} - Q_{22}Q_{41}}{Q_{22}Q_{44} - Q_{24}Q_{42}} \tag{12}$$

$$t_{ss} = \left.\frac{E_s^t}{E_s^i}\right|_{E_p^i=0} = Q_{11} + \frac{Q_{12}(Q_{24}Q_{41} - Q_{21}Q_{44}) + Q_{14}(Q_{21}Q_{42} - Q_{22}Q_{41})}{Q_{22}Q_{44} - Q_{24}Q_{42}} \tag{13}$$

$$t_{sp} = \left.\frac{E_p^t}{E_s^i}\right|_{E_p^i=0} = Q_{31} + \frac{Q_{32}(Q_{24}Q_{41} - Q_{21}Q_{44}) + Q_{34}(Q_{21}Q_{42} - Q_{22}Q_{41})}{Q_{22}Q_{44} - Q_{24}Q_{42}} \tag{14}$$

$$r_{ps} = \left.\frac{E_s^r}{E_p^i}\right|_{E_s^i=0} = \frac{Q_{24}Q_{43} - Q_{23}Q_{44}}{Q_{22}Q_{44} - Q_{24}Q_{42}} \tag{15}$$

$$r_{pp} = \left.\frac{E_p^r}{E_p^i}\right|_{E_s^i=0} = \frac{Q_{23}Q_{42} - Q_{22}Q_{43}}{Q_{22}Q_{44} - Q_{24}Q_{42}} \tag{16}$$

$$t_{ps} = \left.\frac{E_s^t}{E_p^i}\right|_{E_s^i=0} = Q_{13} + \frac{Q_{12}(Q_{24}Q_{43} - Q_{23}Q_{44}) + Q_{14}(Q_{23}Q_{42} - Q_{22}Q_{43})}{Q_{22}Q_{44} - Q_{24}Q_{42}} \tag{17}$$

$$t_{pp} = \left.\frac{E_p^t}{E_p^i}\right|_{E_s^i=0} = Q_{33} + \frac{Q_{32}(Q_{24}Q_{43} - Q_{23}Q_{44}) + Q_{34}(Q_{23}Q_{42} - Q_{22}Q_{43})}{Q_{22}Q_{44} - Q_{24}Q_{42}} \tag{18}$$

Here, r_{ss} and r_{pp} are the *direct* reflection coefficients measuring the reflected waves with polarizations conserved, whereas r_{sp} and r_{ps} are the cross-reflection coefficients denoting the reflected waves with polarizations converted. Similarly, t_{ss} and t_{pp} are the *direct* transmission coefficients, while t_{sp} and t_{ps} denote the cross-transmission coefficients. In the absence of anisotropy where Q matrix is block-diagonalized (i.e., $Q_{13} = Q_{14} = Q_{23} = Q_{24} = Q_{31} = Q_{41} = Q_{32} = Q_{42} = 0$), the polarization-converted terms become exactly zero, $r_{sp} = r_{ps} = t_{sp} = t_{ps} = 0$, and the polarization-conserved coefficients recover those derived for the isotropic case [56]:

$$r_{ss} = -Q_{21}/Q_{22} \tag{19}$$

$$t_{ss} = Q_{11} - Q_{12}Q_{21}/Q_{22} \tag{20}$$

The analytical forms of the coefficients defined in Eqs. (11)–(18) are usually too complicated to derive for an arbitrary anisotropic layered system so that one needs to perform numerical computations.

3 Manipulate EM wave polarizations by metamaterials – reflection geometry

3.1 Single air/metamaterial interface

We first investigate the EM wave scatterings by an interface between air and an anisotropic metamaterial. Although the assumption of a semi-infinite sample is not quite realistic, this is the simplest model to study which yields several analytical results, from which many physical insights can be gained. Unlike the reflection by an isotropic interface that conserves the polarization, here, in the presence of anisotropy, an incident wave with a definite polarization could generate a reflected wave with another polarization because of the fact $r_{sp}, r_{ps} \neq 0$. Define a polarization conversion ratio (PCR) as:

$$\mathrm{PCR} = |r_{sp}|^2/(|r_{ss}|^2 + |r_{sp}|^2) \tag{21}$$

which measures the energy portion transformed from the original polarization, assumed as the s polarization for definiteness, to the other polarization (p polarization) after reflection. Obviously, this ratio depends on the direction (θ, ϕ) of the incident wave vector $\boldsymbol{k}_{\mathrm{in}}$, which is given by $\boldsymbol{k}_{\mathrm{in}} = (\omega/c)[\sin\theta\cos\phi\hat{x} + \sin\theta\sin\phi\hat{y} + \cos\theta\hat{z}]$.

Consider the normal incidence case ($\theta = 0°$), which can be solved analytically. While ϕ is meaningless to define, the direction of $\boldsymbol{k}_{\mathrm{in}}$ in this case, it is still meaningful to differentiate two polarizations. In consistency with the $\theta \neq 0°$ case [57], we define that the s-polarized wave has $\boldsymbol{E}||\hat{e}_s = (-\sin\phi\hat{x} + \cos\phi\hat{y})$ and the p-polarized one has $\boldsymbol{E}||\hat{e}_p = (\cos\phi\hat{x} + \sin\phi\hat{y})$ in the case of $\theta = 0°$. Straightforward calculations yield that

$$r_{sp} = \frac{(\sqrt{\varepsilon_x}\sqrt{\mu_x} - \sqrt{\varepsilon_y}\sqrt{\mu_y})\sin(2\phi)}{(\sqrt{\varepsilon_y} + \sqrt{\mu_x})(\sqrt{\varepsilon_x} + \sqrt{\mu_y})} \tag{22}$$

$$r_{ss} = \frac{\sqrt{\mu_x}\sqrt{\mu_y} - \sqrt{\varepsilon_x}\sqrt{\varepsilon_y} + (\sqrt{\varepsilon_x}\sqrt{\mu_x} - \sqrt{\varepsilon_y}\sqrt{\mu_y})\cos(2\phi)}{(\sqrt{\varepsilon_y} + \sqrt{\mu_x})(\sqrt{\varepsilon_x} + \sqrt{\mu_y})} \tag{23}$$

Several interesting conclusions were obtained through analyzing Eqs. (21)–(23). First, it is shown that all these quantities only depend on ε_x, ε_y μ_x, and μ_y but have nothing to do with ε_z and μ_z since here we only study the normal incidence situation. Second, the polarization conversion effect disappears ($r_{sp} \equiv 0$) in the

absence of anisotropy ($\mu_x = \mu_y = \mu, \varepsilon_x = \varepsilon_y = \varepsilon$), and the reflection coefficient becomes

$$r_{ss} = \frac{\sqrt{\mu}/\sqrt{\varepsilon} - 1}{\sqrt{\mu}/\sqrt{\varepsilon} + 1} \tag{24}$$

recovering the standard result for an isotropic case [1].

With the anisotropy tuned on, r_{sp} could take a nonzero value, but the polarization conversion effect is strongly dependent of the parameter ϕ. When $\phi = 0°$ or $\phi = 90°$, one finds rigorously that $r_{sp} \equiv 0$, indicating the polarization conversion effect vanishes. This is reasonable since both $\boldsymbol{E}$ and $\boldsymbol{H}$ field of the incident wave are *parallel* to a coordinate axis so that the EM wave cannot detect the anisotropy of the medium. Meanwhile, the polarization-converted reflectance $|r_{sp}|^2$ is maximized when $\phi = 45°$. However, a complete polarization conversion (i.e., PCR = 1) does not necessarily appear at $\phi = 45°$, since the polarization-conserved reflectance $|r_{ss}|^2$ is also a function of ϕ. Recalling the definition of PCR in Eq. (20), we find that realizing PCR = 1 requires that $r_{ss} = 0$, leading to the following condition:

$$\cos(2\phi) = \frac{\sqrt{\mu_x}\sqrt{\mu_y} - \sqrt{\varepsilon_x}\sqrt{\varepsilon_y}}{\sqrt{\varepsilon_y}\sqrt{\mu_y} - \sqrt{\varepsilon_x}\sqrt{\mu_x}} \tag{25}$$

Equation (25) shows that, for any value of ϕ, one can always choose appropriate material constants ε_x, ε_y, μ_x, and μ_y to achieve a complete polarization conversion effect.

Numerical calculations were performed to illustrate the above analytical results. Since all metamaterials are intrinsically frequency dispersive, the metamaterial under study was assumed to have the following typical response functions:

$$\mu_x = 1 + \frac{70}{12.71^2 - f^2}, \quad \mu_y = 1 + \frac{22}{6.80^2 - f^2} \tag{26}$$
$$\varepsilon_x = \varepsilon_y = \varepsilon_z = \mu_z = 1$$

where f is the linear frequency measured in GHz. The calculated results of r_{sp}^2, r_{ss}^2, and PCR are shown in Fig. 2(a), (b), and (c), as functions of frequency calculated with different values of ϕ. It is found that the reflectance (both r_{sp}^2 and r_{ss}^2) are significantly enhanced around the two resonance frequencies [6.8 GHz, 12.71 GHz, see Eq. (26); here, the resonance frequencies are belong to microwave spectrum radar bands, which can be taken on arbitrary values in principle], and the polarization-converted reflectance r_{sp}^2 is the largest at $\phi = 45°$, in consistency with our above theoretical analysis. An interesting observation is that while the PCR can reach 1 at some particular frequencies for $\phi = 45°, 75°$, the same is *not* true for $\phi = 5°, 15°$. To understand this point, we put the frequency-dependent forms of ε_x, ε_y, μ_x, and μ_y [Eq. (26)] into Eq. (25) to calculate the value of ϕ at which a complete polarization conversion effect is realized and depicted the curve $\phi \sim f$ in Fig. 3. Indeed, for the model adopted here, there exists a specific regime of polarization angle ($21° - 76°$) inside which a complete polarization conversion effect is realizable via adjusting frequency. For the sake of simplifications, the material losses in all the models for microwave frequency regime have been neglected [see Eqs. (26)–(28) and (31)]. It is found from numerical calculations that all qualitative conclusions drawn in this paper remain unchanged after adding losses to the materials. In particular, while the reflection coefficients r_{ss}, r_{sp} are sensitive to the material losses, the PCR value is relatively robust against the losses.

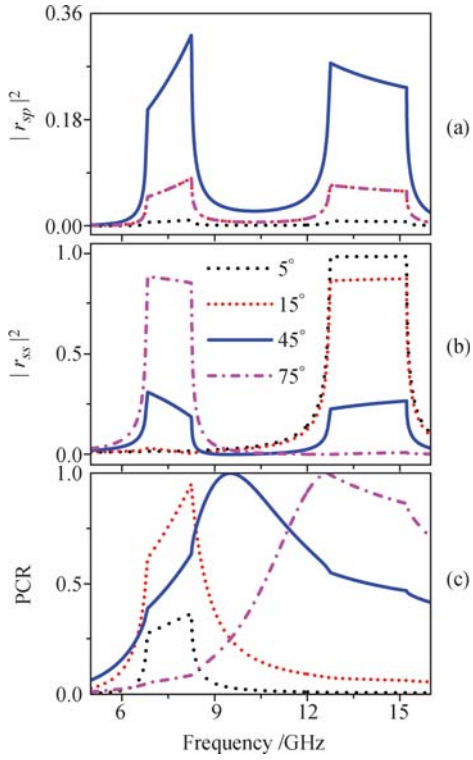

Fig. 2 r_{sp}^2, r_{ss}^2, and PCR as functions of frequency for different values of ϕ, when EM waves are incident from air on the surface of a semi-infinite anisotropic metamaterial medium.

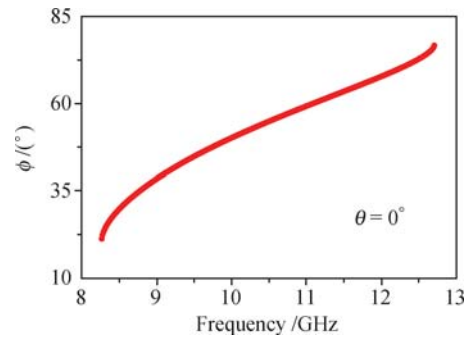

Fig. 3 Relation between the polarization angle ϕ and frequency f, at which a complete polarization conversion effect (PCR = 1) is realizable for the single-interface model.

We next study the oblique angle incidence case, which is much more complex. Figure 4 (a) shows the calculated PCR as a function of f and ϕ, with θ fixed as $\theta = 15°$.

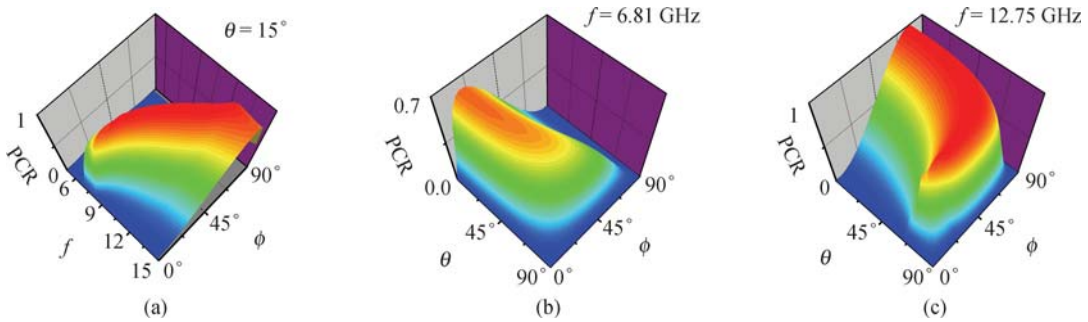

Fig. 4 **(a)** PCR as a function f and ϕ with $\theta = 15°$, calculated for the single-interface model. PCR as a function of θ and ϕ with $f = 6.81$ GHz **(b)** and with $f = 12.75$ GHz **(c)** for the single-interface model.

It is observed that the trajectory connecting those maximum PCR points looks very similar to the $\phi \sim f$ curve, as shown in Fig. 3, which is calculated in the normal incidence case. The physics is that both of them are dictated by the frequency dispersion of the material [Eq. (26)]. Fixing the frequency as $f = 6.81$ GHz and 12.75 GHz, the PCR as functions of θ and ϕ were calculated and depicted the patterns in Fig. 4(b) and (c), respectively. It is noted that the PCR cannot reach 1 in oblique angle incidence case. For $f = 6.81$ GHz, the value of ϕ to realize a maximum PCR increases toward 90° as θ increases, indicating that at glancing incidence, one can rotate $\boldsymbol{H}$ toward $\hat{y}$ to maximize the polarization conversion effect. An opposite behavior of ϕ was found for another resonance [see Fig. 4(c)], since the resonances at $f = 6.8$ GHz and $f = 12.71$ GHz belong to different directions.

3.2 Anisotropic metamaterial slabs

Although the single-interface model is intuitive, it is not quite realistic in practice. In this subsection, we study how to manipulate the EM wave polarizations by anisotropic metamaterial slabs, which are practically realizable. Two examples were given to illustrate the applications of the 4×4 TMM, and brute-force FDTD simulations on specifically designed samples were performed to verify all predictions based on the 4×4 TMM.

The first example is a 1.6-mm-thick metamaterial slab possessing magnetic responses along two in-plane directions:

$$\begin{aligned}\mu_x &= 1 + \frac{15}{12.49^2 - f^2} + \frac{100}{25.73^2 - f^2}\\ \mu_y &= 1+\frac{10}{7.11^2-f^2}+\frac{110}{14.8^2 - f^2}+\frac{220}{22.12^2 - f^2}\\ \varepsilon_x &= \varepsilon_y = \varepsilon_z = \mu_z = 1\end{aligned} \tag{27}$$

With all material and geometrical parameters known, we employed the 4×4 TMM to study the EM wave scatterings by such a slab. Figure 5(a) shows the calculated results of r_{sp}^2 and r_{ss}^2 versus frequencies for normal incidence with $\phi = 45°$. The corresponding PCR are shown in Fig. 5(b) denoted by solid stars. It is found that the spectrum calculated for a finite-thickness slab resembles that of a single-interface case (see Fig. 2) in many respects, although the details of the two spectra are quite different. For example, the reflectance, including both r_{sp}^2 and r_{ss}^2, reach their maximum values at the two resonance frequencies, but the PCR reach their maximums at different frequencies at which r_{ss}^2 are minimized.

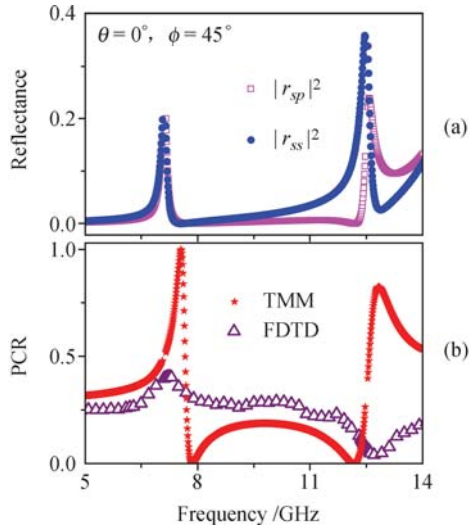

Fig. 5 **(a)** For sample I, the calculated r_{sp}^2 and r_{ss}^2 as functions of frequency under the normal incidence condition with $\phi = 45°$. **(b)** PCR as a function of frequency, obtained by the 4×4 TMM (*solid stars*) and FDTD simulations (*open triangles*) for the realistic metallic structure with unit cell depicted in Fig. 7(a).

We now study the second example, which is a metamaterial slab of the same thickness but possesses magnetic response only along one direction:

$$\begin{aligned}\mu_y &= 1+\frac{10}{7.06^2 - f^2}+\frac{110}{14.54^2 - f^2}+\frac{220}{22.56^2 - f^2}\\ \varepsilon_x &= \varepsilon_y = \varepsilon_z = \mu_x = \mu_z = 1\end{aligned} \tag{28}$$

We employed the 4×4 TMM to study the scatterings by such a metamaterial slab and depicted the normal-incidence spectra of r_{sp}^2, r_{ss}^2, and PCR in Fig. 6, calculated with different values of ϕ. While Fig. 6(a) and (b) show that the spectra of r_{sp}^2, r_{ss}^2 are quite similar to those calculated for sample I, here, the PCR spectrum shown in Fig. 6(c) for sample II looks quite unusual. In particular, the PCR is solely determined by the polarization angle ϕ but is independent of frequency although

the metamaterial is highly dispersive [see Eq. (28)].

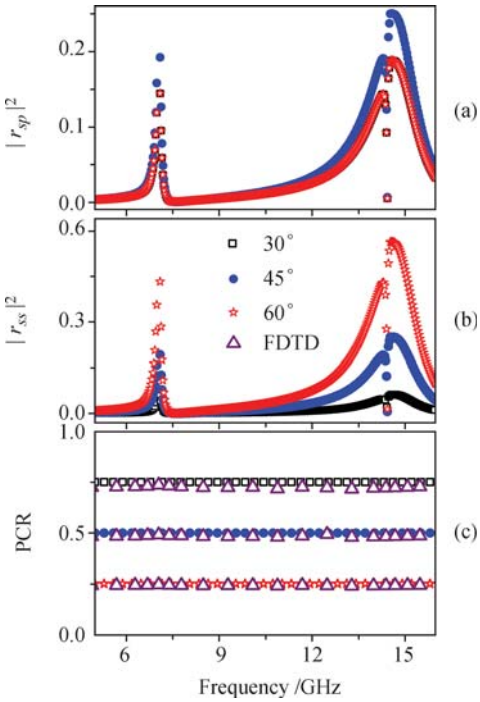

Fig. 6 For Sample II, the calculated **(a)** r_{sp}^2 and **(b)** r_{ss}^2 as functions of frequency under the normal incidence condition with different azimuth angle ϕ. **(c)** PCR versus frequency calculated under the normal incidence condition with different values of ϕ, obtained by the 4×4 TMM (*open squares*, *solid circles*, *open stars*) and the FDTD simulation (*open triangles*) for the realistic metallic structure with unit cell depicted in Fig. 7(b).

To understand such an intriguing phenomenon, we have derived analytical expressions for the reflection coefficients of such a slab under the normal incidence condition [38]. Although the expressions of r_{ss}, r_{sp} [see Eqs. (37) and (38) in Ref. [38]] appear quite complicated, one can still gain a lot of physical insights via analyzing them. We found that $r_{sp} = 0$ in the cases of $\phi = 0°, 90°$, due to the same reasons explained in the single-interface case. In addition, in the case of $\phi = 90°$ where the property is solely determined by ε_x and μ_y, it is easily obtained:

$$r_{ss} = \frac{(\mu_y - \varepsilon_x)\sin(k_{z3}d)}{-2\mathrm{i}\sqrt{\varepsilon_x}\sqrt{\mu_y}\cos(k_{z3}d) + (\varepsilon_x + \mu_y)\sin(k_{z3}d)} \tag{29}$$

which again goes back to the reflectance calculated for an isotropic slab.

The most interesting result appears when the condition $\varepsilon_x = \varepsilon_y = \mu_x \neq \mu_y$ is satisfied. In this case, while both r_{ss} and r_{sp} strongly depend on the value of μ_x, μ_y, and d, such dependences cancel each other in the expression of the PCR. Specifically, through straightforward calculations we found that

$$\mathrm{PCR} = \frac{\sin^2(2\phi)}{4\sin^4\phi + \sin^2(2\phi)} = \cos^2\phi \tag{30}$$

in the case of $\phi \neq 0°$. It is noted that the PCR cannot be defined in the case of $\phi = 0°$.

This peculiar property explains the intriguing behaviors of the PCR, as shown in Fig. 6(c), since the material properties of sample II [$\varepsilon_x = \varepsilon_y = \mu_x = 1$, see Eq. (28)] obviously satisfy the condition $\varepsilon_x = \varepsilon_y = \mu_x \neq \mu_y$. This intriguing behavior could find some applications in reality, in case that one wants to get a broad band polarization manipulation effect in practice.

FDTD simulations [38, 58] were performed to verify these theoretical predictions obtained with the 4×4 TMM. With the help of FDTD simulations, two realistic metallic structures have been designed that exhibit the different material responses, as shown in Eqs. (27) and (28). As depicted in Fig. 7(a) and (b), the unit cell of sample is composed of two split-ring resonators (SRR) [14, 59–61] of different sizes, which are perpendicular to each other, while that of sample II consists of only one single SRR. Repeat the unit cells along the $x(y)$ direction with periodicity 8 mm (5 mm), and then, two 1.6-mm-thick slabs corresponding to the two samples specified by Eqs. (27) and (28) have been obtained. The EM wave normal transmission spectra through the two samples were calculated through the FDTD simulations, and the results were shown by solid lines in Fig. 7(c) and (d) for two independent polarizations ($\boldsymbol{E}||\hat{x}$ and $\boldsymbol{E}||\hat{y}$). Excellent agreements are found between the spectra calculated by the FDTD simulations (*solid lines*) and by the TMM (*open stars*) based on the model systems represented by Eqs. (27) and (28). These excellent agreements demonstrated that our designed structures can indeed be well described by the effective medium models specified by

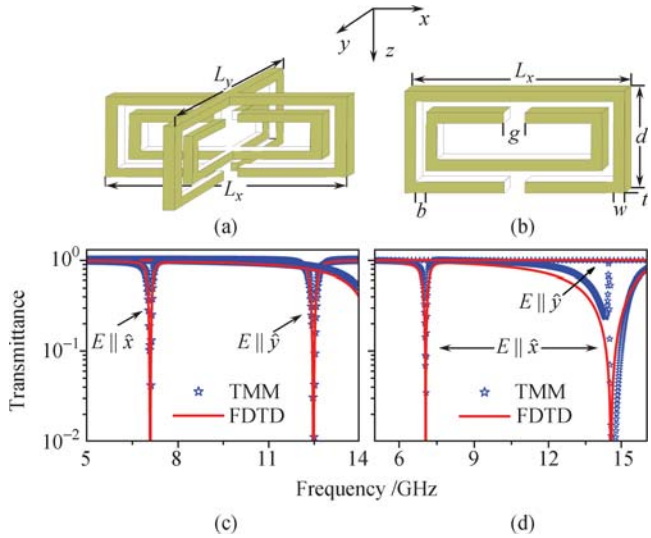

Fig. 7 **(a)** Geometry of the unit cell of Sample I, with parameters given by $L_x = 7.4$ mm, $L_y = 4$ mm. Other details are the same as Sample II. **(b)** Geometry of the unit cell of Sample I, with parameters given by $L_x = 7.4$ mm, $d = 1.6$ mm, $g = 0.4$mm, and $b = w = t = 0.2$ mm. Transmission spectra for Sample I **(c)** and Sample II **(d)** for normally incident EM waves with polarizations $\boldsymbol{E}||\hat{x}$ and $\boldsymbol{E}||\hat{y}$, calculated by the TMM based on the effective-medium models (*open stars*) and the FDTD simulations for realistic structures (*solid lines*).

Eqs. (27) and (28).

We then performed FDTD simulations to calculate the PCR spectra with the designed systems, and showed the results as open triangles in Fig. 5(b) and Fig. 6(c), respectively [38]. Compared with the PCR spectra calculated based on the 4×4 TMM, the agreements are generally quite satisfactory. In particular, we found that the FDTD simulations exactly reproduced the analytical results obtained for sample II [see Eq. (30)], verifying the predictions that sample II can indeed serve as a frequency-independent polarization manipulator. However, the agreement is found to be not perfect near the resonances of sample I. Such discrepancies are probably caused by the finite-size effects since we had to adopt finite-sized samples in our FDTD simulations [38].

3.3 Double-layer metamaterial reflector

From the above discussions for metamaterial slab cases, we find that while the PCR value can be as high as 1, the reflected signal is usually weak ($|r_{sp}| \neq 1$) indicating that the manipulation efficiency is low. The same is true for another type of metamaterial slab with $\vec{\vec{\varepsilon}}$ and $\vec{\vec{\mu}}$ interchanged due to the EM symmetry. The reason is simply that such single-layer slabs are usually not totally reflective for EM waves with arbitrary incidence angles and polarizations.

In this section, we consider a double-layer metamaterial reflector [37] to remedy this problem. Such a reflector consists of a 1.3-mm-thick anisotropic meta-material layer with

$$\begin{aligned} &\mu_x = 1 + \frac{70}{12.71^2 - f^2}, \quad \mu_y = 1 + \frac{22}{6.80^2 - f^2} \\ &\mu_z = 1 \\ &\varepsilon_x = \varepsilon_y = \varepsilon_z = 1 \end{aligned} \tag{31}$$

put on top of a perfect metal sheet (with $\varepsilon_m \to -\infty, \mu_m = 1$). The calculated results of PCR based on the 4×4 TMM are shown as solid lines in Fig. 8(a) for a normal incidence case with $\phi = 45°$ and in Fig. 8(b) for $\theta = \phi = 45°$. It is observed that the PCR is strongly enhanced around two frequencies, ~ 12.7 GHz, ~ 6.8 GHz, corresponding precisely to the two resonances at which μ_x or μ_y tends to infinity [see Eq. (31)]. In particular, for the normal incidence case studied in Fig. 8(a), our theory predicts that PCR = 100% at the two resonance frequencies, indicating that a linearly polarized light converts its polarization completely after the reflection.

In general, both *s*- and *p*-components exist inside the reflected beam. Defining $\Delta\varphi_{sp}$ by $r_{sp}/r_{ss} = |r_{sp}/r_{ss}|e^{i\Delta\varphi_{sp}}$, we calculated $\Delta\varphi_{sp}$ as the functions of frequency for the two cases studied in Fig. 8. From the results (*solid lines*) recorded in Fig. 9, we found that $\Delta\varphi_{sp}$ can take arbitrary values within $[-180°, 180°]$ depending on the frequency (and in turn, on the material parameters), indicating that all possible polarization states (circular, linear, and elliptic) can be realized for the reflected beam. As shown in the illustrations, we picked up four frequencies to calculate the polarization patterns of the reflected beams and found that the resul-

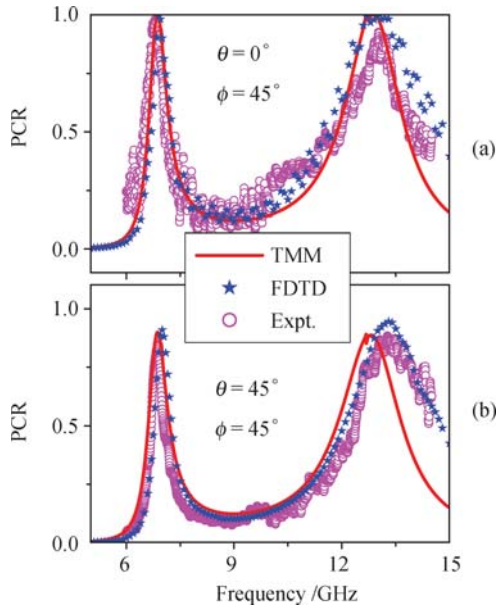

Fig. 8 PCR as the functions of frequency, obtained by TMM calculations on the model system (*solid lines*), FDTD simulations on realistic structures (*solid stars*) and experimental measurements (*open circles*). The incident direction is **(a)** $\theta = 0°, \phi = 45°$ and **(b)** $\theta = \phi = 45°$.

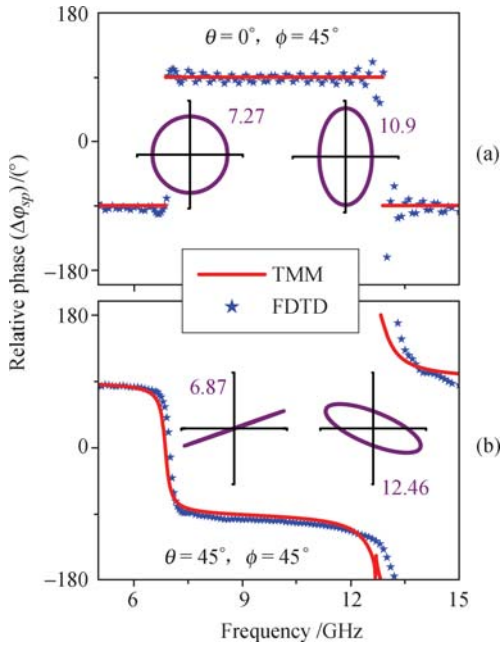

Fig. 9 Frequency dependence of the relative phase $\Delta\varphi_{sp}$ between the *s*- and *p*-polarized modes inside the reflected beam, calculated by TMM on model systems (*solids lines*) and FDTD simulations on realistic structures (*solid stars*). The incident direction is **(a)** $\theta = 0°, \phi = 45°$, and **(b)** $\theta = \phi = 45°$. The insets show the polarization patterns of the reflected beams calculated at different frequencies.

tant polarizations are linear (6.87 GHz), circular (7.27 GHz), and elliptic (10.9 GHz, 12.46 GHz), correspondingly [37].

The physics underlying these unusual phenomena can be understood by a simple argument. Consider the normal incidence case for simplicity. Suppose the incident wave is given by $\boldsymbol{E}^{\text{in}} = (E_x\hat{x} + E_y\hat{y})\,\mathrm{e}^{\mathrm{i}(-\omega z/c+\omega t)}$, then after reflection by an ordinary material, the reflected wave is usually written as $\boldsymbol{E}^r = r\,(E_x\hat{x} + E_y\hat{y})\,\mathrm{e}^{\mathrm{i}(\omega z/c+\omega t)}$ with r being the reflection coefficient. However, in the present case with anisotropy ($\mu_x \neq \mu_y$), the reflection coefficients, r_x, r_y are different for incident waves polarized along two directions. Thus, in general, the reflected wave should be $\boldsymbol{E}^r = (r_xE_x\hat{x} + r_yE_y\hat{y})\mathrm{e}^{\mathrm{i}(\omega z/c+\omega t)}$, and the polarization state can be manipulated through varying r_x, r_y. For the configuration studied in Fig. 8(a) with $E_x = E_y$, if one tune the material parameters to yield $r_x/r_y = -1$, the polarization direction of the reflected wave would be $-\hat{x} + \hat{y}$, which is perpendicular to that of the original wave, $\hat{x} + \hat{y}$. A complete polarization conversion (CPC) is thus realized [37].

The key issue then is how to control r_x and r_y. With the metal sheet on the back, the entire structure is always totally reflective for EM waves, independent of their incidence angles and polarizations, i.e., $|r_x| = |r_y| \equiv 1$. However, the phase $\Delta\psi$ of the reflection coefficient, defined as $r_{x(y)} = \mathrm{e}^{\mathrm{i}\Delta\psi_{x(y)}}$, strongly depends on the metamaterial parameters. The calculated reflection phases $(\Delta\psi_x, \Delta\psi_y)$ for the model system have been depicted in Fig. 10 as functions of frequency. In most cases where $\mu_x(\mu_y)$ is not large, we have $\Delta\psi_{y(x)} \sim \pm 180°$, since the metamaterial layer is transparent and light can directly "see" the metal plate that is reflecting out of phase. However, at the resonances where $\mu_x(\mu_y) \to \pm\infty$, we obtained $\Delta\psi_{y(x)} = 0$ since light is reflected directly by the opaque metamaterial, which possesses infinite impedance [62–64]. In general, any value of $\Delta\psi_{y(x)}$ can be obtained through adjusting the values of $\mu_x(\mu_y)$ and d. The physics for the CPC effect is now clear. Near each resonance, one of μ_x, μ_y becomes very large, while another close to 1, and thus, there must be a frequency where $\Delta\psi_x - \Delta\psi_y = \pm 180°$, and thus, $r_x/r_y = -1$ (see Fig. 10).

We also studied how the effect depends on the incident angles. Depicted in Fig. 11(a) are the PCR as functions of θ and ϕ, calculated at $f = 6.85$ GHz. Numerical computations reveal that the PCR cannot reach 1 in arbitrary incidence case, but the maximum PCR value can still approach 1. As θ increases, we found that the value of ϕ to realize a maximum PCR increases toward 90°, indicating that at glancing incidence, one can rotate $\boldsymbol{E}$ toward $\hat{x}$ to maximize the polarization conversion effect. An opposite behavior of ϕ was found for the resonance at $f = 12.7$ GHz. To facilitate easy comparisons with experiments, the PCR as a function of ϕ with $\theta = 45°$ and as a function of θ with $\phi = 45°$ have been shown in Fig. 5(b) and (c), respectively. It is found that the maximum polarization conversion effect now takes place at $\phi \sim 56°$ when θ is fixed as 45°, different from the normal incidence case. On the other hand, the PCR is a decreasing function of θ when ϕ is fixed as 45° and reaches 1 at $\theta = 0°$.

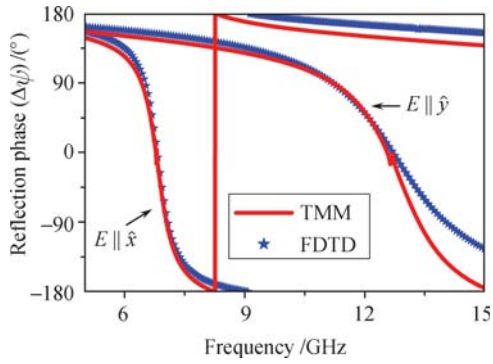

Fig. 10 Frequency dependences of the reflection phase changes $\Delta\psi_{y(x)}$ on the metamaterial reflector surface for normal incident waves with polarizations $\boldsymbol{E}||\hat{x}$ and $\boldsymbol{E}||\hat{y}$, calculated by TMM on model system (*solid lines*) and FDTD simulations on realistic structures (*solid stars*).

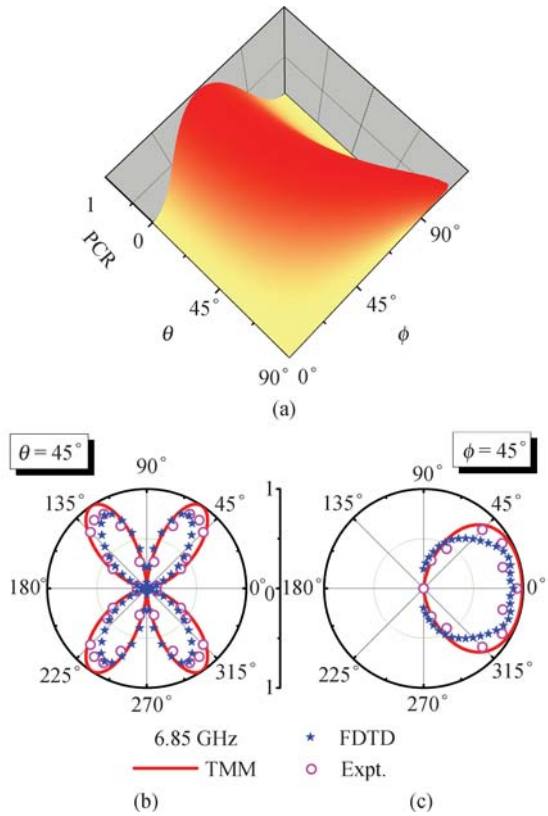

Fig. 11 **(a)** PCR as functions of θ and ϕ, calculated by TMM. **(b)** PCR as a function of ϕ with θ fixed as 45°, obtained by TMM (*solid lines*), FDTD simulation (*solid stars*), and measurements (*open circles*). **(c)** PCR as a function of θ with ϕ fixed as 45°, obtained by TMM (*solid lines*), FDTD simulations (*solid stars*) and measurements (*open circles*). Here, we set $f = 6.85$ GHz.

Microwave experiments and FDTD simulations were performed to demonstrate these predictions. To real-

ize the proposed model system described by Eq. (31), we designed a frequency-selective structure, as shown in Fig. 12(a), which consists of a periodic array of planar H-shaped metallic pattern (lattice constant $a = 7$ mm, thickness = 0.1 mm), printed on a 1.2-mm thick PCB slab (with $\varepsilon_r = 3.6$) with a metal sheet on the back. Other structural parameters are fixed as $b = 5$ mm, $w =$ 1.0 mm. A single H-shaped metallic structure possesses electric resonances for both polarizations [65]. When a metal plate is added, currents are induced on the metal plate surface, flowing along a direction opposite to the currents induced on the H structures. As a result, the entire structure now exhibits magnetic responses with well-defined resonance frequencies, but its electric polarization is strongly diminished since the two currents effectively cancel with each other [66, 67]. The composite material is then perfectly described by the double-layer model [see Eq. (31)], with $d = 1.3$ mm being the thickness of the H-pattern (0.1 mm) plus the inner dielectric layer (1.2 mm) [67]. As a demonstration, we employed FDTD simulations [37] to calculate the reflection phase spectra $(\Delta\psi_x(f), \Delta\psi_y(f))$ of the designed composite material and showed the results in Fig. 10. The good agreement with the model TMM results supports our conclusions.

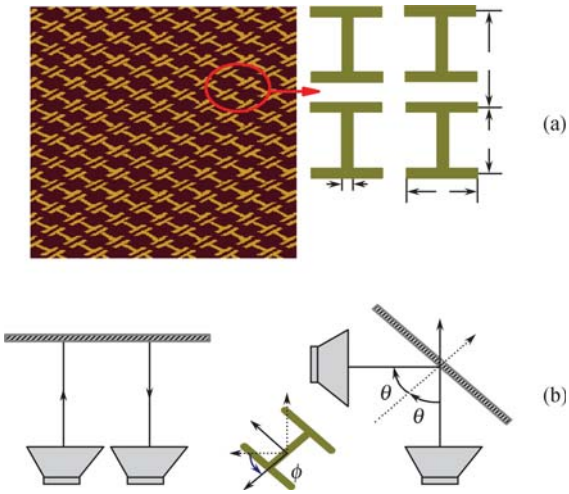

Fig. 12 **(a)** An image of a part of the experimental sample. **(b)** A schematic picture of the experiment setup. Starting from the laboratory coordinate system $\{\hat{x}_0, \hat{y}_0, \hat{z}_0\}$, we first rotate the sample for an angle of θ with respect to the $\hat{y}_0(=\hat{y}_1)$ axis, then show that for an angle of ϕ with respect to the $\hat{z}_1(=\hat{z})$ axis, and finally arrive at the local coordinate system $\{\hat{x}, \hat{y}, \hat{z}\}$ attached to the sample.

A 497 mm × 497 mm sample based on the designs was fabricated to perform the microwave experiments. As schematically shown in Fig. 12(c), the measurements were carried out in an anechoic chamber using a network analyzer (Agilent 8722 ES) and two linearly polarized horn antennas. The distance between the source/receiver antenna and the sample is 6.9 m. The sample was rotated appropriately to achieve a desired incidence angle (θ, ϕ). Illuminating the sample by a linearly polarized signal with $\boldsymbol{E}||\hat{y}_0$ (i.e., s wave), we then measured the reflected signal using a $\hat{y}_0$-polarized receiver horn (data collected as $|r_{ss}|^2$) and an $\hat{x}_0$-polarized one (data collected as $|r_{sp}|^2$). PCR was calculated with the measured $|r_{ss}|^2$ and $|r_{sp}|^2$, and the results were drawn in Fig. 8(a) and (b) as open symbols. FDTD simulations were also performed to calculate the PCR spectra based on the designed system, and the results were shown as solid stars in the same figures. Quantitative agreements are found among the results obtained by the TMM, the FDTD simulations, and experiments. In particular, both experiments and simulations verified the CPC effects predicted by the model analysis. FDTD simulations were subsequently performed to compute the relative phase spectra $(\Delta\varphi_{sp}(f))$. The FDTD results are again in good agreement with the model TMM results, as shown in Fig. 9, indicating that any desired EM wave polarization can be obtained. Finally, experiments and simulations were carried out to study the angle dependences of the polarization conversion effects, and the measured and simulated results were depicted in Fig. 11(b) and 11(c). Satisfactory agreements are noted compared with the model TMM results.

3.4 Optical activity in a metamaterial without chirality

When a linearly polarized light travels through a medium, the polarization direction is rotated by a certain angle during wave propagation. This phenomenon is known as the optical activity [2]. Conventional medium to possess optical activity include chiral media and gyrotropic media, which typically exhibit (imaginary) off-diagonal constitutional tensor elements.

In this section, we demonstrate that our double-plate reflector, which is neither chiral nor gyrotropic, possesses strong optical activity. Specifically, we found that the polarization direction of a linearly polarized incident EM wave can be rotated by an *arbitrary* angle after reflections at our double-layer metamaterial reflector [38]. We now review our results in some details.

Rewrite the reflection coefficients as $r_{ss} = |r_{ss}|e^{i\varphi_s}$, $r_{sp} = |r_{sp}|e^{i\varphi_p}$, the reflected waves can be rewritten as:

$$\boldsymbol{E}_r(\boldsymbol{r}, t) = (|r_{ss}|e^{i\Delta\varphi_{sp}}\hat{e}_s + |r_{sp}|\hat{e}_p)e^{i\varphi_p}e^{-i(\boldsymbol{k}_r\cdot\boldsymbol{r}-\omega t)} \quad (32)$$

where the incident wave is assumed to be s-polarized, $\boldsymbol{k}_r$ is the wave-vector of the reflected wave, and $\Delta\varphi_{sp} = \varphi_s - \varphi_p$ denotes the relative phase between the s- and p-polarized modes inside the reflected beam. One can easily find from Eq. (31) that the reflected wave still takes a linear polarization if the condition

$$\Delta\varphi_{sp} = 0 \quad \text{or} \quad 180^\circ \quad (33)$$

is fulfilled, but the polarization direction is rotated by an angle

$$\Delta\Theta = \arctan\frac{|r_{sp}|}{|r_{ss}|} \tag{34}$$

as compared to that of the original wave. When the condition PCR = 1 is reached implying that $|r_{ss}| = 0$, it is obtained that $\Delta\Theta = 90°$, indicating the original s-polarization has been completely changed to the p-polarization after the reflection [4, 38].

To illustrate how the condition (33) is met, numerical calculations using the 4×4 TMM were performed on the model system described by Eq. (31). Again, first, consider the normal incidence case. Depicted in Fig. 13 is the calculated value of $\Delta\varphi_{sp}$ as functions of frequency and the azimuth angle ϕ. It is noted that the condition ($\Delta\varphi_{sp} = 0$ or $180°$) is satisfied at two frequencies, 6.87 GHz and 12.88 GHz, independent of the parameter ϕ. This fact indicates that the reflected wave still takes a linear polarization at these two frequencies. For the case of oblique angle of incidence ($\theta \neq 0°$), extensive numerical computations were performed, and we found that the condition (33) can still be met at the vicinities of the two frequencies – 6.87 GHz and 12.88 GHz.

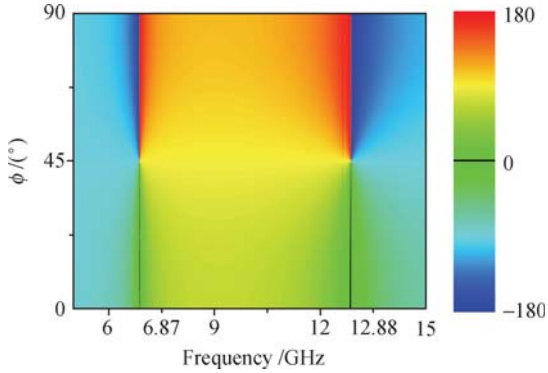

Fig. 13 For the double-plate reflector model $\Delta\varphi_{sp}$ as functions of frequency and the azimuth angle ϕ calculated with the 4×4 TMM under the normal incident condition.

We chose one of those two frequencies to quantitatively study the rotation angle $\Delta\Theta$ based on Eq. (34). Setting $f = 6.87$ GHz, we calculated $|r_{sp}|$ and $\Delta\Theta$ as functions of θ and ϕ and drew the results in Fig. 14(a) and (b). We found that the pattern for $\Delta\Theta$ resembles that of $|r_{sp}|$ very much, and both of them are very complicated functions of the incidence angle specified by θ and ϕ. The most important observation is that an *arbitrary* rotation angle $\Delta\Theta$ can be obtained via adjusting the incidence direction or, equivalently speaking, via rotating the reflector appropriately. This fact indicates that one can *freely* rotate the polarization direction of a linearly polarized light by using our metamaterial reflector. This is remarkable. Although the similar polarization-rotation effect can be achieved based on the gyrotropic (Faraday) effect [68], a thick medium is usually required to achieve a large rotation angle, and also, the efficiency is relatively low. In contrast, such the reflector is much thinner than wavelength and the performance is remarkable.

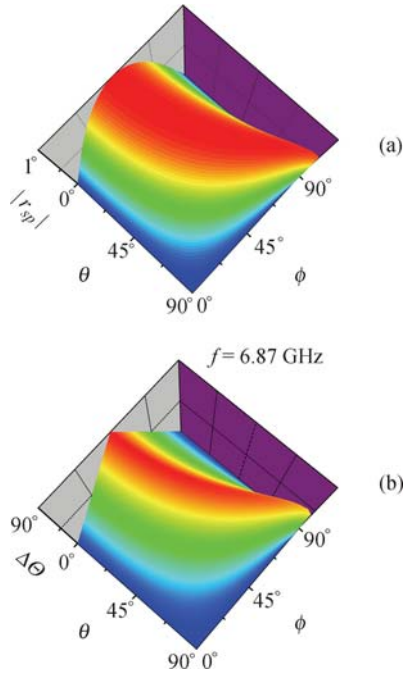

Fig. 14 For the double-plate reflector model, values of $|r_{sp}|$ **(a)** and $\Delta\Theta$ **(b)** as functions of θ and ϕ calculated with the 4×4 TMM setting $f = 6.87$ GHz.

Although the pattern of $\Delta\Theta \sim \theta, \phi$ appears quite complicated, for $\Delta\Theta$, in the case of normal incidence ($\theta = 0°$), an analytical formula can be still derived, with which many new understandings can be gained. In such a case, the incident s-polarized EM wave is given by

$$\begin{aligned}\boldsymbol{E}_{\rm in}(\boldsymbol{r},t) &= (-\sin\phi\hat{x} + \cos\phi\hat{y})\mathrm{e}^{-\mathrm{i}(\omega z/c-\omega t)}\\ \boldsymbol{H}_{\rm in}(\boldsymbol{r},t) &= (-\cos\phi\hat{x} - \sin\phi\hat{y})\mathrm{e}^{-\mathrm{i}(\omega z/c-\omega t)}\end{aligned} \tag{35}$$

A unique property in such a situation is that the EM wave can be separated as two independent linearly polarized waves:

$$\begin{aligned}\begin{pmatrix}\boldsymbol{E}_{\rm in}(\boldsymbol{r},t)\\ \boldsymbol{H}_{\rm in}(\boldsymbol{r},t)\end{pmatrix} &= -\sin\phi\begin{pmatrix}\hat{x}\\ \hat{y}\end{pmatrix}\mathrm{e}^{-\mathrm{i}(\omega z/c-\omega t)}\\ &\quad + \cos\phi\begin{pmatrix}\hat{y}\\ -\hat{x}\end{pmatrix}\mathrm{e}^{-\mathrm{i}(\omega z/c-\omega t)}\end{aligned} \tag{36}$$

For each of these two linearly polarized waves, the reflection coefficients, denoted by r_x and r_y, could take different values. Since the Maxwell equations are linear ones, the reflected wave must be

$$\boldsymbol{E}_r(\boldsymbol{r},t) = (-r_x\sin\phi\hat{x} + r_y\cos\phi\hat{y})\,\mathrm{e}^{\mathrm{i}(\omega z/c+\omega t)} \tag{37}$$

With a perfect-metal slab on the back, such double-layer reflector is always totally *reflecting*, that is, the amplitudes of the reflection coefficients r_x and r_y are always absolutely 1, but their phases could be different. Therefore, when the condition

$$r_x/r_y = -1 \tag{38}$$

is satisfied, the reflected wave still takes a linear polarization [Note that the condition (38) is applicable only to the case of normal incidence, but the condition (33)

is valid in a general situation]. As the condition (38) is satisfied, the $\boldsymbol{E}$ vector of the reflected wave would be $\boldsymbol{E}_r \sim -\sin\phi\hat{x} - \cos\phi\hat{y}$. As schematically shown in Fig. 15, such an $\boldsymbol{E}$ vector has been rotated by an angle

$$\Delta\Theta = \begin{cases} 2\phi, & 0^\circ < \phi \leqslant 45^\circ \\ 180^\circ - 2\phi, & 45^\circ < \phi < 90^\circ \end{cases} \quad (39)$$

with respect to that of the incident wave, $\boldsymbol{E}_{\rm in} \sim -\sin\phi\hat{x} + \cos\phi\hat{y}$. Equation (39) thus provides us a rigorous and analytical formula to calculate the polarization rotation angle under the normal incidence condition. Indeed, the $\Delta\Theta \sim \phi$ relation calculated by the 4×4 TMM is shown by solid stars in Fig. 16, which is in excellent agreement with the analytical relation Eq. (39) represented by a solid line.

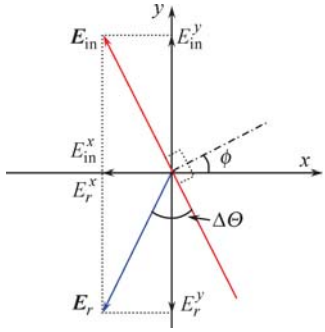

Fig. 15 Schematic picture showing relationships among the $\boldsymbol{E}_{\rm in}$ vector of the incident wave, the $\boldsymbol{E}_r$ vector of the reflected wave, and the polarization rotation angle $\Delta\Theta$, when an EM wave normally strikes on the double-plate meta material reflector.

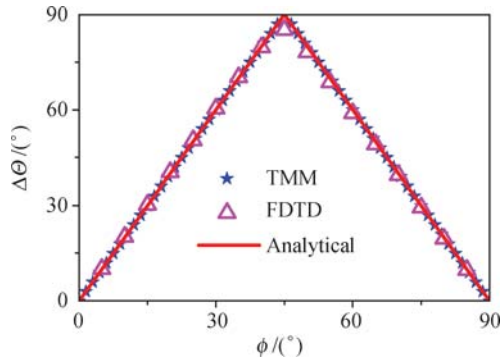

Fig. 16 The polarization rotation angle $\Delta\Theta$ as a function of ϕ, calculated under the normal incidence condition by the 4×4 TMM (*solid stars*) on the model system, analytical relation Eq. (38) (*solid lines*), and the FDTD simulations (*open triangles*) on the realistic system.

Again, these theoretical predictions were successfully verified by FDTD simulations on realistic structures [38]. The calculated results of $\Delta\Theta$ are shown in Fig. 16 as a function of the polarization angle ϕ, represented by open triangles. Perfect agreements were found between the FDTD simulations and the model TMM results, as well as the analytical relation Eq. (39).

3.5 Manipulate wave polarizations at visible frequencies

Although many fascinating applications were theoretically proposed for metamaterials and some of them were successfully realized at microwave frequencies (including the polarization manipulation effects mentioned in this section), very few were experimentally confirmed at optical frequencies. This is due to the significantly enhanced challenges faced by both experiment and theory at optical frequencies. In this section, we review our recent efforts in designing and fabricating appropriate optical metamaterials and demonstrating their strong abilities to control light polarizations at visible frequencies [39].

As schematically shown in Fig. 17(a), the designed metamaterial consists of a layer of gold rod array and a continuous gold film, separated by a SiO_2 layer. This trilayer structure was fabricated layer-by-layer with electron beam evaporation of constituent materials. The 15-nm-thick gold layer was first deposited on a GaAs substrate with 1 nm Titanium as the adhesive layer and then covered by a 60 nm SiO_2 separation layer. The top gold rod array, with a thickness of 15 nm, was fabricated with standard electron-beam lithography and lift-off technique. Each gold rod is sized 240 nm × 60 nm, and the periodicities of the array are 300 nm and 150 nm along two directions. A series of samples based on the designs were fabricated with sizes fixed as 100 μm×100 μm. Figure 17(b) shows a scanning electron microscopy (SEM) picture of one typical sample.

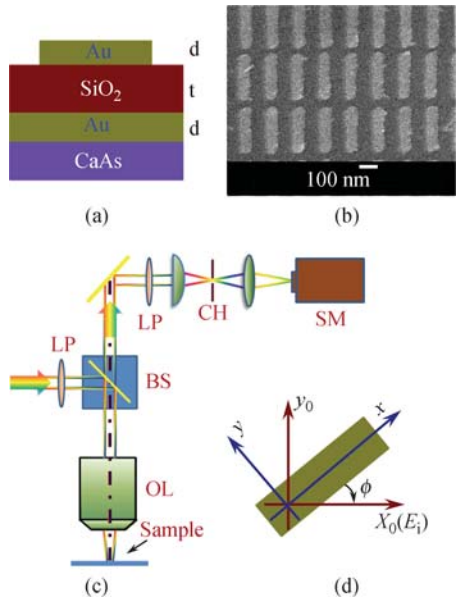

Fig. 17 **(a)** Side-view geometry of the optical metamaterial studied in this paper. **(b)** Top-view SEM picture of part of the experimental sample. **(c)** Scheme of the experimental setup. Here, BS – beam splitter; CH – confocal hole; LP – linear polarizer; OL – objective lens; SM – spectrometer. **(d)** The coordinate system adopted in this paper.

Optical experiments were performed to measure the polarization manipulation effects. The experimental setup is schematically depicted in Fig. 17 (c). Halogen tungsten was used as the excitation white light source, which was focused on the sample surface by an objec-

tive lens. The reflected light was collected by the same lens and dispersed on the monochromator. Linear polarizers were inserted in the paths of both the incident and reflected light to control the light polarizations. In our measurements, we set the incident $\boldsymbol{E}$ field parallel to a fixed laboratory axis $\hat{x}_0$ and then rotated the sample to change the incident wave polarization with respect to the sample [see Fig. 17(d)]. With a fixed incident polarization (assumed as the s polarization), we rotated the receiver to measure the reflectance for the reflected signals with the same polarization ($|r_{ss}|^2$) and that with a p polarization ($|r_{sp}|^2$). We first rotated the sample so that the incident $\boldsymbol{E}$ field is parallel to one of the optical axes and measured the direct reflection spectra $|r_{ss}|^2(|r_{sp}|^2 \equiv 0$ in this case). The spectra for $\phi = 0°$ and $\phi = 90°$ cases were depicted in Fig. 18(a) as solid and open symbols, respectively. Both experimental data and simulation results are referenced by the reflection spectrum measured/calculated with a semi-infinite Si slab. As $\lambda > 750$ nm, the relative reflectivity is higher than 1 since our system possesses a higher reflectivity than a Si slab. The spectra clearly show that the designed metamaterial is not totally reflecting, since gold is not a perfect metal at optical frequencies. Therefore, the mechanism for microwave frequencies (Section 3.4) does not work here for the optical metamaterials.

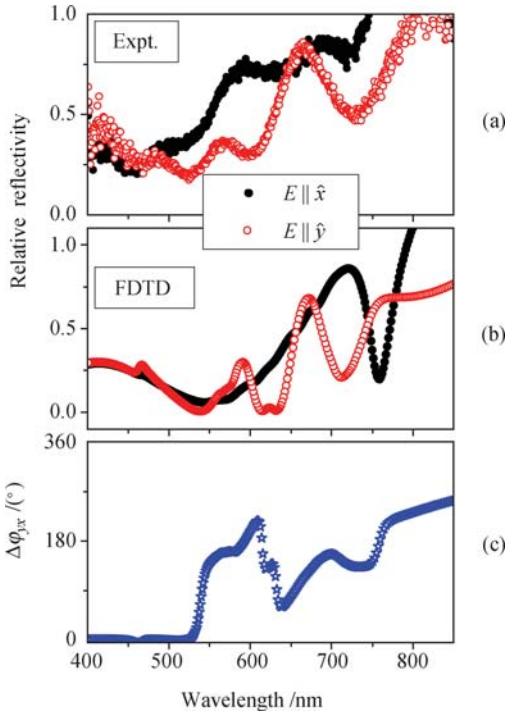

Fig. 18 Relative reflectivity as functions of wavelength for normally incident waves with polarizations $\boldsymbol{E}\|\hat{x}$ (*solid symbols*) and $\boldsymbol{E}\|\hat{y}$ (*open symbols*), obtained by **(a)** measurements and **(b)** FDTD simulations. **(c)** Reflection phase difference $\Delta\varphi_{yx}$ as a function of wavelength calculated by the FDTD simulations.

We then rotated the sample such that $\phi = 45°$ [see Fig. 17(d)]. Since the incident wave is not polarized along one of the optical axes, both $|r_{ss}|^2$ and $|r_{sp}|^2$ are nonzero, and the measured spectra are shown in Fig. 19(a) as solid and open symbols, respectively. Strong polarization-converted reflection signal ($|r_{sp}|^2$) appear around 680 nm, which is even prominently shown in PCR spectra depicted in Fig. 19(b). The maximum PCR value is found as 83% at 680 nm wavelength. We further employed a tunable femtosecond laser as the excitation source to perform the same measurement and depicted the PCR spectra in Fig. 19(b) as solid stars. The PCR value obtained with laser input is significantly enhanced, and the maximum PCR value is as high as 96% at 685 nm. This is easy to understand, since a laser beam has a much better directionality than a focused white light beam.

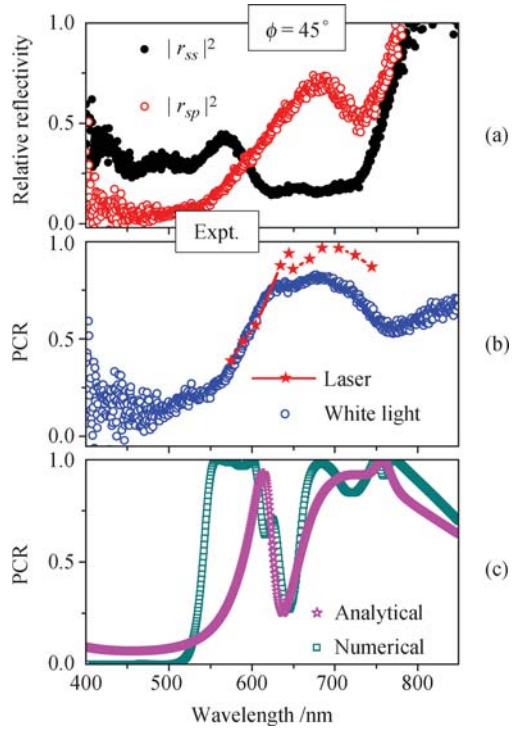

Fig. 19 **(a)** Measured polarization-conserved relative reflectivity ($|r_{ss}|^2$, *solid symbols*) and polarization-converted relative reflectivity ($|r_{sp}|^2$, *open symbols*) as functions of wavelength. **(b)** The calculated PCR as a function of wavelength using the experimental data. **(c)** The PCR spectra as functions of wavelength obtained by numerical simulations and theoretical analysis.

FDTD simulations were performed to understand these intriguing phenomena [39]. In our simulations, the permittivity of gold is taken as $\varepsilon = 9.0 - (1.37 \times 10^{16})^2/[\omega^2 + \mathrm{i}(1.0027 \times 10^{14})\omega]$, the refractive index of SiO_2 is 1.5, and the permittivity of the semi-infinite GaAs substrate is 10.8. Direct reflection spectra for $\phi = 0°$ and $\phi = 90°$ cases were first calculated, and the calculated reflectance spectra ($|r_x|^2$ and $|r_y|^2$) were depicted in Fig. 18(b). Reasonable agreements were found when compared with the experimental spectra, and most experimental features were reproduced. Besides the reflectance, FDTD calculations also provided us the information of reflection phase. In Fig. 18(c), where the calculated reflection phase difference for two

polarizations ($\Delta\psi_{yx} = \psi_y - \psi_x$) is shown as a function of wavelength, we found that $\Delta\varphi_{yx}$ approaches 180° within the range of 650–760 nm, coinciding with the frequency range where the PCR peak is found [see Fig. 19(b)]. In fact, by decoupling the incident wave to two independent polarizations, the PCR spectra can be calculated for arbitrary ϕ case (under normal incidence) using the following formula:

$$\mathrm{PCR} = \frac{[|r_x|\sin\phi - |r_y|\cos\phi\cos(\Delta\varphi_{yx})]^2}{[|r_x|\cos\phi + |r_y|\sin\phi\cos(\Delta\varphi_{yx})]^2 + [|r_x|\sin\phi - |r_y|\cos\phi\cos(\Delta\varphi_{yx})]^2} \tag{40}$$

The PCR spectra thus calculated is shown in Fig. 19(c) as open squares for $\phi = 45°$, which is in reasonable agreement with the measured spectra. A straightforward explanation of the large polarization conversion effect is that, around 680 nm wavelength, one has similar reflectance for two linear polarizations (i.e., $|r_x| \approx |r_y|$) but with nearly 180° reflection phase difference.

We found that the inherent physics behind such unusual phenomena is quite different from microwave one since the metal has a finite penetration length here. This is reinforced by Fig. 18(a) where the reflectance is not 100%. Therefore, the above double-layer effective medium model (Section 3.4) is not suitable for the present system. Instead, we found that it is better to model the present system as a single-layer effective medium with effective permittivity $\tilde{\varepsilon}$ and permeability $\tilde{\mu}$, since the considered wavelength ~700 nm is much larger than the total thickness of the structure 90 nm. Effective optical parameters were retrieved [9, 69] using the FDTD simulated transmission/reflection coefficients, and the retrieved values of $\tilde{\varepsilon}_x$, $\tilde{\varepsilon}_y$, $\tilde{\mu}_x$, and $\tilde{\mu}_y$ were plotted in Fig. 20(a)–(d). To better understand the role of resonances, we employed standard Lorentz models to fit the retrieved effective parameters and finally obtained the following analytical formulas:

$$\begin{aligned}
\varepsilon_x &= 4 - \frac{656^2}{f^2 + i\cdot 2\cdot f} + \frac{520^2}{205^2 - f^2 - i\cdot 17.5\cdot f} \\
&\quad + \frac{90^2}{400^2 - f^2 - i\cdot 17\cdot f} \\
\varepsilon_y &= 3.3 - \frac{655^2}{f^2 + i\cdot 2\cdot f} + \frac{180^2}{450^2 - f^2 - i\cdot 19\cdot f} \\
\mu_x &= 1 + \frac{310^2}{350^2 - f^2 - i\cdot 130\cdot f} \\
\mu_y &= 1.1 + \frac{135^2}{160^2 - f^2 - i\cdot 25\cdot f} + \frac{65^2}{391^2 - f^2 - i\cdot 17\cdot f}
\end{aligned} \tag{41}$$

where f denotes the frequency in THz. The effective parameters calculated based on Eq. (41) are shown in Fig. 4(e)–(h) as functions of frequency. It is interesting to note that, beside the common Drude-like contributions in ε_x and ε_y that originate from the material itself, formulas (41) imply that a series of additional EM resonances exist in such a metamaterial. The magnetic resonances are induced by an antisymmetric coupling of the currents flowing in the two metallic layers, which are similar to those found at microwave frequencies [37, 67]. For the electric resonances, the electric current in each gold rod is *parallel* to that flowing in the continuous gold film, forming a symmetric mode [70, 71]. In general, these EM resonances occur at different wavelengths that are dictated by the *anisotropic* geometric structures. Thus, our system is ideal anisotropic optical material possessing wide parameter tunability so that it can fulfill many applications with appropriate designs. The PCR spectrum was calculated employing the generalized 4×4 TMM with effective parameters given by Eq. (41). The results depicted in Fig. 19(c) as open stars are shown in reasonable agreements with both the direct numerical results and the experimental data.

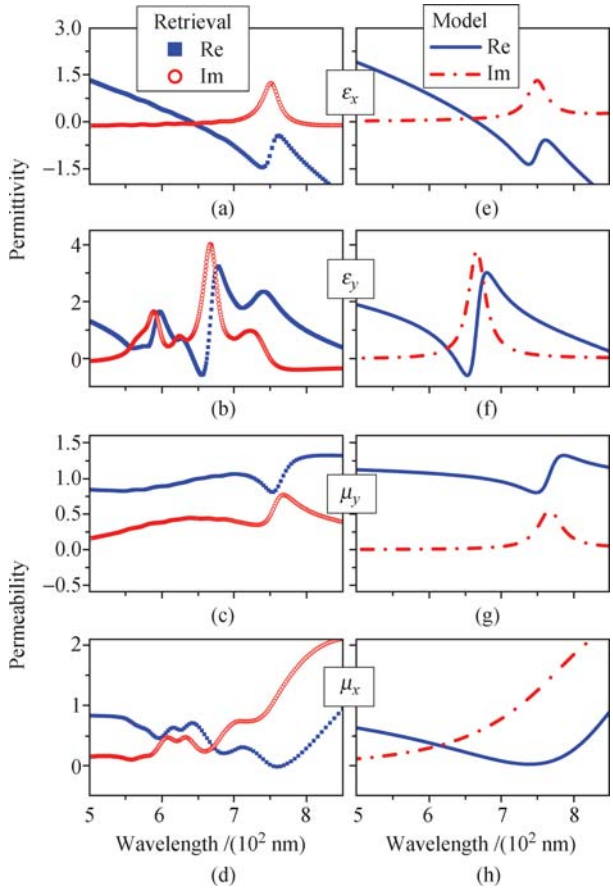

Fig. 20 Retrieved effective parameters of the metamaterial, **(a)** $\tilde{\varepsilon}_x$, **(b)** $\tilde{\varepsilon}_y$, **(c)** $\tilde{\mu}_y$, and **(d)** $\tilde{\mu}_x$, as functions of wavelength; Optical parameters **(e)** $\tilde{\varepsilon}_x$, (f) $\tilde{\varepsilon}_y$, **(g)** $\tilde{\mu}_y$, and **(h)** $\tilde{\mu}_x$ as functions of wavelength, calculated with formulas (40).

The analytical model offers us a physical picture on the polarization manipulation effect. From the definition of PCR, it is noted that PCR=1 requires $r_{ss} = 0$. While it

is difficult to analyze the expression of r_{ss} for a metamaterial slab [Eq. (38) in Ref. [38]], we found it very helpful and intuitive to analyze r_{ss} of an air/metamaterial interface [Eq. (30) in Ref. [38]]. The condition of $r_{ss} = 0$ rigorously leads to an analytical formula

$$Z_x \cdot Z_y = 1 \tag{42}$$

in the case of $\phi = 45°$. Here, $Z_x = \sqrt{\mu_y}/\sqrt{\varepsilon_x}$ and $Z_y = \sqrt{\mu_x}/\sqrt{\varepsilon_y}$ are the impedance for light polarized along x and y directions. In fact, since the normal reflection coefficients are $r_x = (Z_x - 1)/(Z_x + 1)$ and $r_y = (Z_y - 1)/(Z_y + 1)$ for two polarizations, when the condition (42) is met, one can easily verify that $r_x = -r_y$ so that PCR = 1 at $\phi = 45°$. The condition Eq. (42) has a clear physical implication: the two directions must satisfy an EM reciprocal principle in order to realize a complete polarization conversion at $\phi = 45°$. A limiting solution of Eq. (42) is that $Z_x \to 0, Z_y \to \infty$, indicating that the system behaves as a *perfect electric conductor* (PEC) for x-polarized light but as a *perfect magnetic conductor* (PMC) for y-polarized light. This is just the situation realized in a microwave frequency regime (Section 3.4). At higher frequencies, however, metal is no longer perfect so that one cannot achieve a PEC or a PMC. However, Eq. (42) shows that those EM resonances [as shown in Eq. (41)] can be tuned to generate appropriate optical parameters that satisfy the EM symmetry. When the latter is achieved, a high polarization conversion effect can be realized. To test this picture, the real and imaginary parts of $Z_x \cdot Z_y$ as functions of wavelength were plotted in Fig. 21(b), compared with the PCR spectra replotted in Fig. 21(a). As expected, it is found that $Z_x \cdot Z_y \approx 1$ at two wavelengths 628 nm and 766 nm, which directly explains the two PCR peaks observed both experimentally and theoretically in Fig. 5(a), (b), and (c). We note that the condition (42), obtained based on a single air/metamaterial interface, is not rigorously applicable to the present slab case. This also explains why the measured PCR cannot reach 1. Nevertheless, we found condition (42) is intuitive to understand the inherent physics and is helpful for future designs of similar systems.

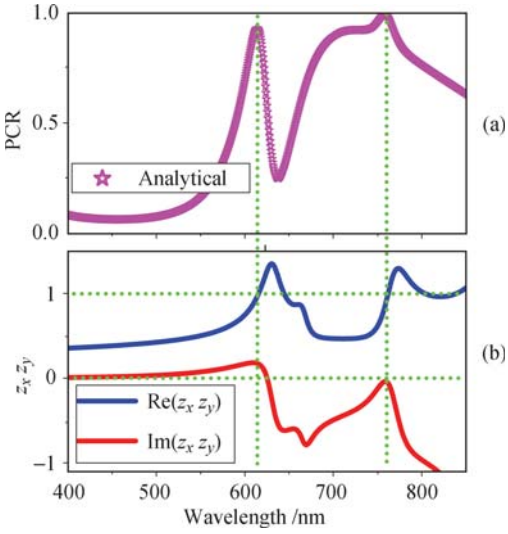

Fig. 21 **(a)** The PCR spectrum as a function of wavelength obtained by theoretical analysis. **(b)** Real and imaginary parts of $Z_x \cdot Z_y$ as functions of wavelength.

4 Manipulate EM wave polarizations by metamaterials – transmission geometry

In aforementioned sections, we reviewed the recent efforts in employing metamaterials to control EM wave polarizations based on the reflection geometry. Similar effects can be realized based on a transmission geometry, which will be briefly reviewed in this section.

Quite recently, there have been several studies of creating metamaterial transmission polarizers [40–47]. Chin *et al.* proposed to use an anisotropic metamaterial slab as a transmission polarizer [40], in which the function and the transmission efficiency of the polarizer can be designed and controlled. The metamaterial is composed by electric inductance-capacitance (ELC) resonator particles, which exhibit designable effective electric permittivity. It was found that a transmission polarizer consisting of two-layer ELC can convert a linearly polarized wave to a circularly polarized one, while a four-layer ELC transmission polarizer can convert the polarization of a linearly polarized wave from one direction to it cross direction. On the other hand, Beruete *et al.* combined the ideas of extraordinary optical transmission and metamaterials to successfully fabricate a polarization device that can select and rotate EM wave polarizations [41]. For an input wave with arbitrary polarization, any polarization can be attained at the output by just adjusting the number of stacked plates. The most attractive feature of such a device is that the phase shift between two orthogonal eigenwaves is achieved with the negative and positive indices of refraction for two independent linearly polarized waves. T. Q. Li *et al.* studied the propagations of microwaves through a chiral metamaterial [42], which is an array of magnetic dimmers made of two square single split-ring resonators (SSRRs). The optical activity of such a medium is originated from the hybridization effect of magnetic resonances. T. Li *et al.* investigated the near infrared optical transmissions through a silver film with L-shaped holes array [43]. Besides the enhanced transmission due to the combined plasmonic excitations, nearly 45° polarization rotation was observed with relative strong transmissions for a polarized light with a specific incidence angle at the wavelength $\sim$ 1200 nm. It is a giant optical rotation rate considering that the sample is only 80 nm thick. Plum *et al.* reported that very strong optical activity can be observed in artificial planar metamaterials based on an array of asymmetrically

split rings without chirality at all [44]. Both microwave and optical experiments were performed to demonstrate this effect [44].

5 Conclusions

In summary, we have briefly reviewed the recent efforts in manipulating EM wave polarizations based on the metamaterial concept. We first established a generalized 4×4 transfer-matrix method to study the scatterings of EM waves by layered anisotropic metamaterials in a general case, and then, we employed this method to study the polarization manipulation effects under the reflection geometry with several different metamaterial systems, including an anisotropic metamaterial interface, an anisotropic metamaterial slab, a double-layer metamaterial reflector, and an optical metamaterial. We showed that several amazing polarization-related phenomena can be realized by metamaterials, including the polarization conversion, the polarization rotation, and so on. We also briefly reviewed the existing efforts of polarization manipulation under the transmission geometry, which were mainly carried out in other research groups. Many of these interesting phenomena were verified by FDTD simulations and experiments at both microwave and visible frequencies. These remarkable properties have promised metamaterials a lot of technological applications, and further studies are needed to explore more fascinating new physics and applications of metamaterials with respect to the polarization control.

Acknowledgements This work was supported by the National Natrual Science Foundation of China (Grant Nos. 60725417 and 60990321), the State Key Development Program for Basic Research of China (973 project) (Grant No. 2006CB921506), and Shanghai Science and Technology Committee. M. Qiu was supported by the Swedish Foundation for Strategic Research (SSF) through the Future Research Leaders program and the Swedish Research Council (VR).

References

1. M. Born and E. Wolf, Principles of Optics, Cambridge: Cambridge University Press, 1999
2. E. Hecht, Optics, New York: Addison Wesley, 2002
3. J. A. Kong, Electromagnetic Wave Theory, Cambridge: EMW Publishing, 2005
4. J. M. Bennett and H. E. Bennet, in: Handbook of Optics, Sec. 10, edited by W. G. Driscoll and W. Vaughan, New York: McGraw-Hill, 1978
5. J. B. Pendry, A. J. Holden, W. J. Stewart, and I. Youngs, Phys. Rev. Lett., 1996, 76: 4773
6. J. B. Pendry, A. J. Holden, D. J. Robbins, and W. J. Stewart, IEEE Trans. Microwave Theory Tech., 1999, 47: 2075
7. D. R. Smith, Willie J. Padilla, D. C. Vier, S. C. Nemat-Nasser, and S. Schultz, Phys. Rev. Lett., 2000, 84: 4184
8. H. O. Moser, B. D. F. Casse, O. Wilhelmi, and B. T. Saw, Phys. Rev. Lett., 2005, 94: 063901
9. S. Zhang, W. Fan, N. C. Panoiu, K. J. Malloy, R. M. Osgood, and S. R. J. Brueck, Phys. Rev. Lett., 2005, 95: 137404
10. V. M. Shalaev, W. Cai, U. K. Chettiar, H. Yuan, A. K. Sarychev, V. P. Drachev, and A. V. Kildishev, Opt. Lett., 2005, 30: 3356
11. G. Dolling, C. Enkrich, M. Wegener, C. M. Soukoulis, and S. Linden, Opt. Lett., 2006, 31: 1800
12. G. Dolling, M. Wegener, C. M. Soukoulis, and S. Linden, Opt. Lett., 2007, 32: 53
13. V. G. Veselago, Sov. Phys. Usp., 1968, 10: 509
14. R. A. Shelby, D. R. Smith, and S. Schultz, Science, 2001, 292: 77
15. D. R. Smith, J. B. Pendry, and M. C. K. Wiltshire, Science, 2004, 305: 788
16. J. B. Pendry, Phys. Rev. Lett., 2000, 85: 3966
17. N. Fang, H. Lee, C. Sun, and X. Zhang, Science, 2005, 308: 534
18. A. Ono, J. Kato, and S. Kawata, Phys. Rev. Lett., 2005, 95: 267407
19. P. A. Belov, Y. Hao, and S. Sudhakaran, Phys. Rev. B, 2006, 73: 033108
20. X. H. Hu, Z. H. Hang, J. Li, J. Zi, and C. T. Chan, Phys. Rev. E, 2006, 73: 015602
21. C. Y. Luo, M. Ibanescu, E. J. Reed, S. G. Johnson, and J. D. Joannopoulos, Phys. Rev. Lett., 2006, 96: 043903
22. W. H. Wang, X. Q, Huang, L. Zhou, and C. T. Chan, Opt. Lett., 2008, 33: 369
23. J. Lu, T. Grzegorczyk, Y. Zhang, J. Pacheco Jr., B. I. Wu, J. Kong, and M. Chen, Opt. Express, 2003, 11: 723-734
24. Y. O. Averkov and V. M. Yakovenko, Phys. Rev. B, 2005, 72: 205110
25. B. I. Wu, J. Lu, J. Kong, and M. Chen, J. Appl. Phys., 2007, 102: 114907
26. Z. Y. Duan, B. I. Wu, J. Lu, J. A. Kong, and M. Chen, Opt. Express, 2008, 16: 18479
27. N. Engheta, IEEE Antennas Wireless Propag. Lett., 2002, 1: 10
28. L. Zhou, H. Q. Li, Y. Q. Qin, Z. Y. Wei, and C. T. Chan, Appl. Phys. Lett., 2005, 86: 101101
29. H. Li, J. M. Hao, L. Zhou, Z. Wei, L. Gong, H. Chen, and C. T. Chan, Appl. Phys. Lett., 2006, 89: 104101
30. U. Leonhardt, Science, 2006, 312: 1777
31. J. B. Pendry, D. Schurig, and D. R. Smith, Science, 2006, 312: 1780
32. A. J. Ward and J. B. Pendry, J. Mod. Opt., 1996, 43: 773
33. M. Rahm, D. Schurig, D. A. Roberts, S. A. Cummer, D. R. Smith, and J. B. Pendry, Photon. Nanostruct. Fundam. Appl., 2008, 6: 87
34. H. Y. Chen and C. T. Chan, Appl. Phys. Lett., 2007, 90: 241105
35. M. Yan, W. Yan, and M. Qiu, Phys. Rev. B, 2008, 78: 125113
36. T. Yang, H. Y. Chen, X. D. Luo, and H. R. Ma, Opt. Express, 2008, 16: 18545
37. J. M. Hao, Y. Yuan, L. Ran, T. Jiang, J. A. Kong, C. T.

Chan, and L. Zhou, Phys. Rev. Lett., 2007, 99: 063908
38. J. M. Hao and L. Zhou, Phys. Rev. B, 2008, 77: 094201
39. J. M. Hao, Q. J. Ren, Z. H. An, X. Q. Huang, Z. H. Chen, M. Qiu, and L. Zhou, Phys. Rev. A, 2009, 80: 023807
40. J. Y. Chin, M. Z. Lu, and T. J. Cui, Appl. Phys. Lett., 2008, 93: 251903
41. M. Beruete, M. Navarro-Cía, M. Sorolla, and I. Campillo, J. Appl. Phys., 2008, 103: 053102
42. T. Q. Li, H. Liu, T. Li, S. M. Wang, F. M. Wang, R. X. Wu, P. Chen, S. N. Zhu, and X. Zhang, Appl. Phys. Lett., 2008, 92: 131111
43. T. Li, H. Liu, S. M. Wang, X. G Yin, F. M. Wang, S. N. Zhu, and X. Zhang, Appl. Phys. Lett., 2008, 93: 021110
44. E. Plum, X. X. Liu, V. A. Fedotov, Y. Chen, D. P. Tsai, and N. I. Zheludev, Phys. Rev. Lett., 2009, 102: 113902
45. J. Yelk, M. Sukharev, and T. Seideman, J. Chem. Phys., 2008, 129: 064706
46. J. X. Cao, H. Liu, T. Li, S. M. Wang, T. Q. Li, S. N. Zhu, and X. Zhang, J. Opt. Soc. Am. B, 2009, 26: B96
47. J. Y. Chin, J. N. Gollub, J. J. Mock, R. P. Liu, C. Harrison, D. R. Smith, and T. J. Cui, Opt. Express, 2009, 17: 7640
48. D. R. Smith and D. Schurig, Phys. Rev. Lett., 2003, 90: 077405
49. L. Zhou, C. T. Chan, and P. Sheng, Phys. Rev. B, 2003, 68: 115424
50. S. L. Sun, X. Q. Huang, and L. Zhou, Phys. Rev. E, 2007, 75: 066602
51. L. B. Hu and S. T. Chui, Phys. Rev. B, 2002, 66: 085108
52. Q. Cheng and T. J. Cui, Appl. Phys. Lett., 2005, 87: 1741102
53. T. Jiang, J. M. Zhao, and Y. J. Feng, J. Phys. D: Appl. Phys., 2007, 40: 1821
54. P. Yeh, Optical Wave in Layered Media, New York: Wiley, 1988
55. K. Busch, C. T. Chan, and C. M. Soukoulis, in: Photonic Band Gap Materials, edited by C. M. Soukoulis, Dordrecht: Kluwer, 1996
56. L. Zhou, W. J. Wen, C. T. Chan, and P. Sheng, Phys. Rev. Lett., 2005, 94: 243905
57. For the case of $\theta \neq 0°$, the electric field of s-polarized wave has $\boldsymbol{E}||\hat{e}_s = -\sin\phi\hat{x} + \cos\phi\hat{y}$, and the p-polarized wave has $\boldsymbol{E}||\hat{e}_p = \cos\theta\cos\phi\hat{x} + \cos\theta\sin\phi\hat{y} - \sin\theta\hat{z}$.
58. A. Taflove, Computational Electrodynamics: The Finite-Difference-Time-Domain Method, Norwood: Artech House INC, 2000
59. D. R. Smith, D. C. Vier, N. Kroll, and S. Schultz, Appl. Phys. Lett., 2000, 77: 2246
60. P. Markos and C. M. Soukoulis, Phys. Rev. E, 2002, 65: 036622
61. N. Katsarakis, T. Koschny, and M. Kafesaki, E. N. Economou, and C. M. Soukoulis, Appl. Phys. Lett., 2004, 84: 2943
62. D. Sievenpiper, L. J. Zhang, R. F. J. Broas, N. G. Alexópolous, and E. Yablonovitch, IEEE Trans. Microwave Theory Tech., 1999, 47: 2059
63. F. Yang and Y. Rahmat-Samii, IEEE Trans. Antennas Propag., 2003, 51: 2691
64. H. Mosallaei and K. Sarabandi, IEEE Trans. Antennas Propag., 2004, 52: 2403
65. W. J. Wen, L. Zhou, J. Li, W. Ge, C. T. Chan, and P. Sheng, Phys. Rev, Lett., 2002, 89: 223901
66. L. Zhou, W. J. Wen, C. T. Chan, and P. Sheng, Appl. Phys. Lett., 2003, 83: 3257
67. J. M. Hao, L. Zhou, and C. T. Chan, Appl. Phys. A, 2007, 87: 281
68. L. D. Landau, E. M. Lifshitz, and L.P. Pitaevskii, Electrodynamics of Continuous Media, London: Butterworth-Heinemann Ltd., 1984
69. D. R. Smith, S. Schultz, P. Markos, and C. M. Soukoulis, Phys. Rev. B, 2002, 65: 195104
70. V. A. Podolskiy, A. K. Sarychev, and V. M. Shalaev, J. Nonlinear Opt. Phys. Mater., 2002, 11: 65
71. Uday K. Chettiar, A. V. Kildishev, T. A. Klar, and V. M. Shalaev, Opt. Express, 2006, 14: 7872